Point defect induced incommensurate dipole moments in the $KCa_2Nb_3O_{10}$ Dion-Jacobson layered perovskite

J. Kong [1], S. K. Nayak [2], K. Co,[2] S. Nayak,[1,*] J. Wu,[1] A. Feteira [3], K. A. Beyer,[4] S. P. Alpay,[2,5] and A. Pramanick [1,†]

[1]*Department of Materials Science and Engineering, City University of Hong Kong, Hong Kong SAR, China*
[2]*Department of Materials Science and Engineering, University of Connecticut, Storrs, Connecticut 06269, USA*
[3]*Materials and Engineering Research Institute, Sheffield Hallam University, Sheffield S1 1WB, United Kingdom*
[4]*Advanced Photon Source, Argonne National Laboratory, Lemont, Illinois 60439, USA*
[5]*Department of Physics, University of Connecticut, Storrs, Connecticut 06269, USA*

(Received 10 May 2021; revised 2 August 2021; accepted 30 November 2021; published 16 December 2021)

Local structural distortions due to isolated atomic defects and defect complexes strongly affect the macroscopic properties of oxide ceramics. While the characterization of local defect structures is more common in simple ABO_3 perovskites, unambiguous determination of the same in layered perovskites is more difficult due to their complex crystal structures. Here, we combined x-ray pair distribution function and density functional theory calculations to characterize the structure of cation-oxygen divacancy pairs in a Dion-Jacobson (D-J) layered perovskite. Our results indicate that local incommensurate dipole moments with polarization density in the range of $\sim$0.1–17 $\mu C/cm^2$ are created due to divacancy-induced structural distortions in the D-J phase $KCa_2Nb_3O_{10}$. This is comparable with defect dipole moments observed in well-known perovskite ferroelectrics. The current results imply that controlling the atomic defects can potentially lead to significant control of dielectric properties in D-J layered perovskites.

DOI: 10.1103/PhysRevB.104.224104

I. INTRODUCTION

Interest in layered perovskites has grown in recent years due to their functionalities such as high-k dielectrics, high T_C superconductors, catalysis, and quantum magnetism [1–5]. The unique properties of layered perovskites can be attributed to their two-dimensional slab structure, whereby discrete ABO_3 perovskitelike layers are separated by interlayer structural motifs such as alkali metal ions or Bi_2O_2 fluorite units. Dion-Jacobson (D-J) phases are one such class of layered perovskites with the general formula of $A'[A_{m-1}B_mO_{3m+1}]$, where A' is an alkali metal and m represents the number of octahedral layers within each perovskite slab [6–8]. In recent years, D-J phase oxides have gained attention due to their numerous existing and potential applications, such as tunable and high-temperature dielectrics, photocatalysis, photovoltaic electrode materials, and next-generation of high-temperature superconductors [9–14]. Furthermore, discovery of ferroelectric instability in some D-J phase oxides and D-J phase oxide-derived nanosheets has broadened the application range of these materials [15,16]. Despite several experimental studies of the crystal structure of D-J phases, the exact determination of their atomic structure can be difficult due to complex local structural distortions [17–21]. In this regard, a critical source of local structural distortions is point defects such as cation or oxygen vacancies, which result as an unintended consequence of high-temperature processing and may have a significant impact on material properties. Indeed, earlier studies indicated that local electrical dipoles and structural distortions arising from point defects significantly influence functional properties of ABO_3 perovskites, such as electrical polarization and dielectric relaxation [22,23]. It is also acknowledged that cation and oxygen vacancies may influence functional properties of D-J phases, such as electrical conductivity, dielectric permittivity, and photocatalytic activity [24–27]. To better understand the effect of atomic-scale defects on macroscopic properties, it is essential to characterize the local structure of the defect centers. However, detailed characterization of local defect structures in D-J phase compounds is currently lacking.

Characterization of local structural distortions due to atomic defects has remained a challenging task. In the past, local defect structures in ABO_3 perovskite ferroelectrics were characterized using techniques such as electron paramagnetic resonance (EPR) or positron annihilation spectroscopy [28–34], which nevertheless have their own limitations. EPR can be used only for paramagnetic ions. Positron annihilation spectroscopy can infer characteristic defect types, but the structure of a defect complex is difficult to decipher. Furthermore, microscopic techniques such as high-resolution transmission electron microscopy suffer from surface-related effects and artifacts related to sample preparation. In recent years, efforts have been made to characterize the local structure around defects using the pair distribution function (PDF), derived from total x-ray or neutron scattering experiments [35,36]. However, unambiguous determination of defect structure using the PDF alone can be challenging. Notably, for layered perovskite D-J phases, the presence of four or more elemental components and a sandwich of multiple structural forms open a multitude of possibilities for defects, which complicates the determination of exact local structural

*Present address: Indian Institute of Technology, Madras.
†apramani@cityu.edu.hk

distortions introduced by defects. In this regard, density functional theory (DFT) can narrow the possible space of defect complexes based on energy considerations as well as factoring in local atomic chemistry and charge balance requirements [37–44]. Thus, pairing x-ray scattering data with *ab initio* computations holds significant potential advantages.

Here, we demonstrate the characterization of local defect-induced structural distortions in the prototypical D-J layered perovskite $KCa_2Nb_3O_{10}$ using combination of x-ray total scattering experiments and DFT calculations. Our results indicate the presence of large local dipole moment density due to Ca-O vacancy pairs (or divacancies) in $KCa_2Nb_3O_{10}$, akin to other well-known perovskites such as $PbTiO_3$. The defect-induced local dipoles are likely a contributing factor to the dielectric relaxation and nonlinearity measured for this material. The current result implies that local defect dipoles should be an important factor in discussing the functional properties of D-J phase compounds.

II. EXPERIMENT

$KCa_2Nb_3O_{10}$ ceramics were prepared by a conventional solid-state synthesis method. Stoichiometric amounts of K_2CO_3 (Sigma Aldrich, 99.7%), $CaCO_3$ (Sigma Aldrich, nominal purity 100.0%), Na_2CO_3 (Sigma Aldrich, nominal purity 100.0%), and Nb_2O_5 (Sigma Aldrich, 99.9%) were ball-milled in ethanol for 24 h. The powder samples were dried in the oven at 100 °C for 2 h before weighing to remove adsorbed moisture. The mixed powder slurry was dried and then calcined at ∼1200 °C for 12 h. The calcined powders were ground, mixed with polyvinyl alcohol, and sieved through 100 μm mesh. The granulated powders were pressed into pellets of diameter 10 mm and thickness 1 mm with a pressure ∼34.5 MPa. The pellets were placed in an alumina crucible and sintered in air at 1325 °C for 4 h. During sintering, the green pellets were covered with powders of the same composition of $KCa_2Nb_3O_{10}$ to limit volatilization of certain elements, such as K, Ca, and Nb. The x-ray diffraction pattern of synthesized $KCa_2Nb_3O_{10}$ could be indexed with a D-J phase structure, indicating that we had successfully synthesized the $KCa_2Nb_3O_{10}$ compound with no evident secondary phases (see details in Supplemental Material Sec. A) [45].

The frequency-dependent (100 Hz $\leqslant f \leqslant$ 1 MHz) dielectric properties of $KCa_2Nb_3O_{10}$ at low electric fields (0.1 V ac) were measured using an LCR meter (Agilent-4284A, Technologies). The high-field electrical polarization of the $KCa_2Nb_3O_{10}$ was characterized from polarization-electric field (*P-E*) hysteresis loops using a Radiant Precision LC-II Ferroelectric Test System (2835 Pan American Fwy).

High-energy synchrotron x-ray total scattering data at room temperature were collected at the beamline 11-ID-B of the Advanced Photon Source, Argonne National Laboratory, using x-rays of wavelength $\lambda = 0.2113$ Å. The samples were loaded in Ø1mm quartz capillaries. The scattered intensity was recorded at a sample-to-detector distance of 170 mm with Debye-Scherrer geometry in transmission mode on a large amorphous-Si TFT panel detector. The local structure was characterized from the atomic PDF $G(r)$, obtained from the x-ray total scattering intensity pattern. The high-energy x-ray scattering results were corrected for the sample absorption, background, Compton scattering, and incident flux. The normalized intensities were reduced to the structure factor $S(Q)$, which was then Fourier transformed using the following function:

$$G(r) = \frac{2}{\pi}\int_{Q_{\min}}^{Q_{\max}} Q[S(Q)-1]\sin(Qr)dQ \qquad (1)$$

to achieve the corresponding PDFs, where Q is the momentum transfer and is defined as $Q = 4\pi\sin(\theta)/\lambda$. The PDF conversion was executed in the software PDFGETX2 [46], and the $Q_{\max}$ used was 19 Å^{-1} (see details in Supplemental Material Sec. B) [45]. The PDF was analyzed using the software PDFGUI [47]. The synchrotron x-ray diffraction pattern was analyzed by Rietveld refinement using FULLPROF software [48].

Raman measurements were carried out in a backscattering geometry using a Thermo Scientific DXR™2 Raman microscope equipped with a laser of 532 nm with a maximum power of 10 mW.

III. RESULTS AND DISCUSSION

A. Electrical properties

Figure 1(a) shows the low-field dielectric constant (ε') and dielectric loss ($\tan\delta$) of the $KCa_2Nb_3O_{10}$ ceramics at room temperature as a function of frequency. The dielectric constant is higher for lower frequencies due to contributions from dipolar and interfacial polarization but stabilizes for frequencies $> 10^4$ Hz. Figure 1(b) shows the temperature-dependent dielectric constant and dielectric loss, exhibiting large dielectric relaxation at high temperatures for $KCa_2Nb_3O_{10}$ ceramics. Notably, the dielectric loss for the material used in this study is observed to be lower (∼0.11 at 100 Hz) than in previous studies [9,49]. The high-field dielectric permittivity was characterized from the *P-E* hysteresis loops of $KCa_2Nb_3O_{10}$ ceramics, which were measured with an applied ac electric field of amplitude $E \leqslant 210$ kV/cm and frequency $f = 10$ Hz, as shown in Fig. 1(c). Details for calculation of the high-field permittivity from the *P-E* loops are provided in Sec. C of the Supplemental Material [45] (see also Refs. [50,51] therein). The dielectric permittivity as a function of electric field amplitude is shown in Fig. 1(d). A nonlinear increase in ε' can be observed for electric field amplitudes >180 kV/cm. Such unusual properties, that is, a large dispersion of ε' with frequency and nonlinear increase in ε' with electric field amplitude, can potentially arise in centrosymmetric ionic compounds as a result of relaxation or reorientation of local dipoles created due to point defects [39,52,53]. Compositional analysis of the synthesized $KCa_2Nb_3O_{10}$ powders indicated a significant presence of ionic vacancies (see details in Sec. D of the Supplemental Material [45]). To better understand the vacancy-induced local dipoles for the layered perovskite $KCa_2Nb_3O_{10}$, we undertook a detailed structural characterization of this material.

B. Description of Rietveld and PDF refinements

The Rietveld refinement of the x-ray diffraction data is shown in Fig. 2(a), which indicates that the long-range crystal structure of $KCa_2Nb_3O_{10}$ is orthorhombic with the *Cmcm*

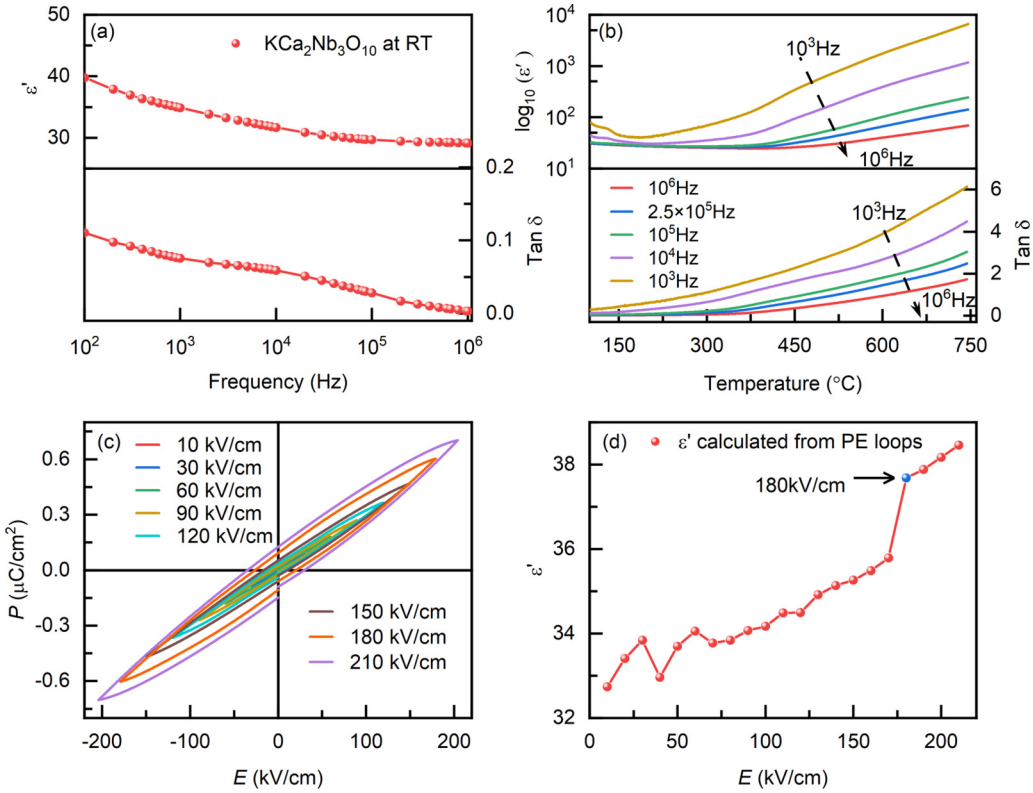

FIG. 1. (a) Frequency-dependent dielectric constant (ε') and loss-tangent ($\tan\delta$) of $KCa_2Nb_3O_{10}$ ceramics at various frequencies; 100 Hz $\leqslant f \leqslant$ 1 MHz at room temperature. (b) Dielectric constant (ε') and loss-tangent ($\tan\delta$) of $KCa_2Nb_3O_{10}$ at higher temperature (100–750 °C). (c) Hysteresis loops (P vs E) of $KCa_2Nb_3O_{10}$ measured at $E \leqslant 210$ kV/cm and $f = 10$ Hz. (d) High electrical field permittivity (calculated from *PE* loops) as a function of an electrical field.

space group and lattice parameters: $a = 3.8787(2)$ Å, $b = 29.5385(15)$ Å, and $c = 7.7219(4)$ Å. For the current refinement, the average crystal structure of the $KCa_2Nb_3O_{10}$ phase determined by Fukuoka *et al.* [54] was used as a starting point (see details in Sec. E 1 of the Supplemental Material [45]). The atomic positions in the long-range average structure are listed in Table I. The corresponding unit cell structure is shown in Fig. 2(b), which is composed of two perovskite slabs of $Ca_2Nb_3O_{10}$ and K ions sandwiched between the perovskite blocks. Both the terminal (next to the K ions) and inner (central) layer octahedra exhibit tilting around the a and b axes at room temperature. The complex crystal structure of $KCa_2Nb_3O_{10}$ has three different cations that are significantly different in terms of their ionic radii and nature of cation-oxygen bonding, which makes local deviations from long-range average structure likely; consider that such local deviations also exist in simple perovskite $BaTiO_3$ with ionic Ba-O and covalent Ti-O bonds [55]. The presence of ionic vacancies is also expected to cause local structural distortions [35]. Therefore, we examined the short-range local atomic structure of $KCa_2Nb_3O_{10}$ from analysis of its x-ray PDF or $G(r)$. The structure parameters obtained from Rietveld refinement were used as a starting point for fitting the x-ray $G(r)$. Figure 2(c) compares the model $G(r)$ based on the average long-range structure and the experimentally observed x-ray PDF. In Fig. 2(c), the model $G(r)$ is calculated by refining only the lattice parameters and the atom displacement parameters (ADPs) to best fit the observed $G(r)$ while keeping the atomic coordinates the same as that obtained from fitting of the Bragg peaks. The experimentally observed $G(r)$ and the calculated $G(r)$ based on the average structure are close to each other for $r > 6$ Å, which indicates that they approximately converge for $r > 6$ Å. However, there are notable differences between the experimental and the calculated $G(r)$ of the average structure for $r < 6$ Å, most prominently in the region marked by a green oval in Fig. 2(c), which has the most contribution from the nearest and the next-nearest neighbor Nb-O, Ca-O, and O-O interatomic correlations (see Fig. S5 in the Supplemental Material [45]). It is known that nearest-neighbor-correlated atomic motions can influence the peak intensity for pairwise atomic correlations in the short range [56,57]. Therefore, we accounted for the effect of correlated atomic motions by refining the displacement correlation parameter δ_2 at low temperatures [58]. In this case, we fitted the experimental $G(r)$ by refining δ_2, in addition to lattice parameters and the ADPs. As shown in Fig. 2(d), including δ_2 in the refinement could reproduce the peak intensity of the nearest-neighbor Nb-O correlations [$\delta_2 = 3.23$ ($4.7e^{-5}$)], which means that atomic motions of Nb and O can be highly correlated. However, the next two peaks Ca-O/O-O in the $G(r)$ cannot be fit well even while refining δ_2, particularly for the shorter Ca-O/O-O distances at $r \sim 2.4$ Å. This can be explained due to the predominantly covalent character of the Nb-O bonds, in contrast to the predominantly ionic Ca-O bonds [57]. Thus, it is difficult to describe the experimentally observed difference between the average and local structures

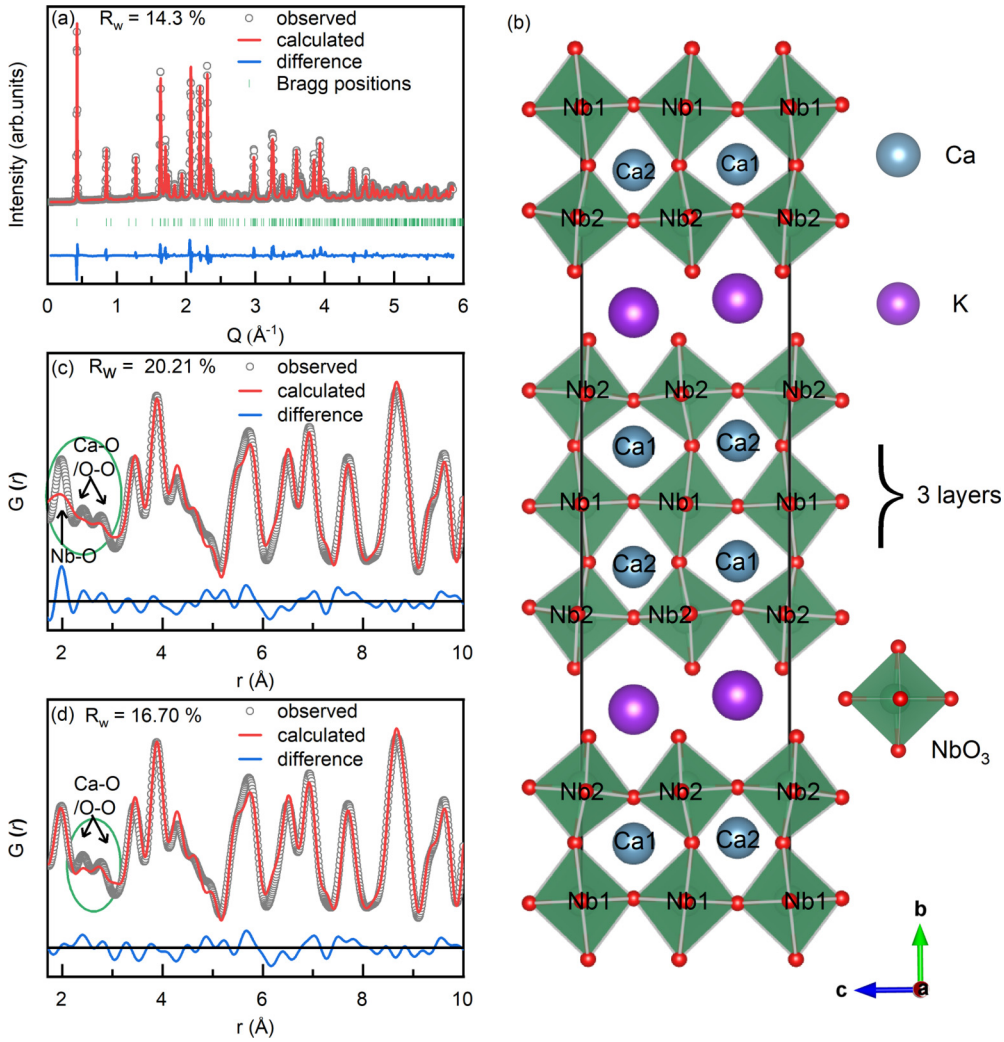

FIG. 2. (a) Synchrotron x-ray diffraction pattern along with the Rietveld refinement of $KCa_2Nb_3O_{10}$. (b)The crystal structure of $KCa_2Nb_3O_{10}$. (c) Observed and calculated $G(r)$ profiles of $KCa_2Nb_3O_{10}$ for interatomic distance $r \leqslant 10$ Å, while refining only lattice parameter and atom displacement parameters (ADPs) of the average structure. (d) Observed and calculated $G(r)$ profiles of $KCa_2Nb_3O_{10}$ for interatomic distance $r \leqslant 10$ Å, while refining displacement correlation parameter δ_2, in addition to lattice parameter and ADPs.

of $KCa_2Nb_3O_{10}$ as a result of correlated dynamic atomic motions alone. Effort to fit the experimental $G(r)$ by undertaking a full refinement of the structure, including lattice parameters, atomic positional coordinates, and APDs, provided a reasonable fit for $r > 6$ Å but also did not provide a good fit in the low-r range covering nearest-neighbor distances (i.e., $r < 6$ Å; details are provided in Sec. E 3 of the Supplemental Material [45]).

It is known that D-J phase compounds are highly amenable to nonstoichiometry [24–27]. X-ray photoelectron spectroscopy (XPS) indicated that Ca and K vacancies are the major defect species in the synthesized powders (see Table S1 in the Supplemental Material [45]). However, the fundamental charge neutrality condition dictates that the cation vacancies should be ideally compensated by anion vacancies, in this case, oxygen vacancies, in the form of cation-oxygen divacancy pairs. This is also supported by the exhibition of good insulating properties of the synthesized ceramics, with a very low dielectric loss at room temperature, as shown in Fig. 1(a), which otherwise may show enhanced electron (hole) conductivity due to excitation of low-lying defect states into the conduction (valence) band. Moreover, due to the complex crystal structure of $KCa_2Nb_3O_{10}$, various types of divacancy configurations are also possible. Therefore, to investigate the most likely isolated vacancy and divacancy complexes, we undertook a detailed characterization of the vacancy and divacancy formation energies for $KCa_2Nb_3O_{10}$ using DFT.

C. DFT computation of defect formation energies

First-principles calculations were performed with DFT using the plane-wave pseudopotential method [59,60]. Non-spin-polarized calculations were performed with the generalized gradient approximation with Perdew-Burke-Ernzerhof parametrization as the exchange-correlation functional [61]. The core and valence electrons were treated with the projector augmented wave method [62]. The kinetic energy cutoff for the plane waves was set to 500 eV. For the defect models, the basis vectors of the unit cell have been expanded to $2 \times 1 \times 2$ supercells containing 256 atoms. Figure 3(a) shows the [100]

TABLE I. Structural parameters, fractional atomic coordinates, and ADPs (U_{iso} in Å^2) from the Rietveld refinement.

Formular $KCa_2Nb_3O_{10}$					
Crystal system: orthorhombic phase					
Space group: *Cmcm*					
Atoms	Site	*X*	*Y*	*Z*	U_{iso}
K1	4*c*	0	0.2589(2)	0.25	0.0056(18)
Ca1	4*c*	0.5	0.0722(3)	0.75	0.014(2)
Ca2	4*c*	0.5	0.0795(3)	0.25	0.025(3)
Nb1	4*a*	0	0	0.5	0.0013(7)
Nb2	8*f*	0	0.1441(5)	0.5034(3)	0.0012(4)
O1[a]	4*c*	0	0.003(3)	0.75	0.198(12)
O2[a]	4*b*	0.5	0	0.5	0.181(10)
O3	8*f*	0	0.0734(7)	0.469(4)	0.096(5)
O4	8*f*	0.5	0.1383(6)	0.520(4)	0.022(3)
O5	4*c*	0	0.1304(12)	0.75	0.004(6)
O6	4*c*	0	0.1430(12)	0.25	0.006(6)
O7	8*f*	0	0.2064(5)	0.533(3)	0.000(3)
Lattice parameter (Å)					
$a = 3.8787(2)$	$b = 29.5385(15)$				
$c = 7.7219(4)$	$\alpha = \beta = \gamma = 90^\circ$				
$R_w = 14.3\%$					

[a]Note that O1 and O2 are disordered atoms [54].

projection of the supercell with all inequivalent atom types indicated by differentiating colors. The atomic positions of defect models were thoroughly optimized to minimize the residual interatomic forces. The integrations in the Brillouin zone were performed in a discretized Monkhorst-Pack [63] *k*-points mesh of 2 × 2 × 2 for the geometrical optimization. Geometrical optimization for the models was carried out with the tolerance for total energy convergence set to 1.0×10^{-7} eV. The calculations were performed with the Vienna *Ab initio* Simulation Package (VASP) [64,65]. The volume-relaxed lattice parameters were found to be $a = 3.95$ Å, $b = 29.98$ Å, and $c = 7.83$ Å, which match with those obtained from our Rietveld refinement of the x-ray diffraction pattern and consistent with earlier studies [54].

The centrosymmetric crystal structure of $KCa_2Nb_3O_{10}$ has one type of K-atom site, two symmetry-inequivalent Ca (Ca1 and Ca2) atom sites, two symmetry-inequivalent Nb (Nb1 and Nb2) atom sites, and seven symmetry-inequivalent O (O1, …, O7) atom sites, see Fig. 3(a). The defect models were created to span all possible isolated vacancies (V_K, V_{Ca1}, V_{Ca2}, V_{Nb1}, V_{Nb2}, V_{O1}, …, V_{O7}), constituting a total of 12 configurations [see the label of Fig. 3(b)], as well as divacancy cases forming

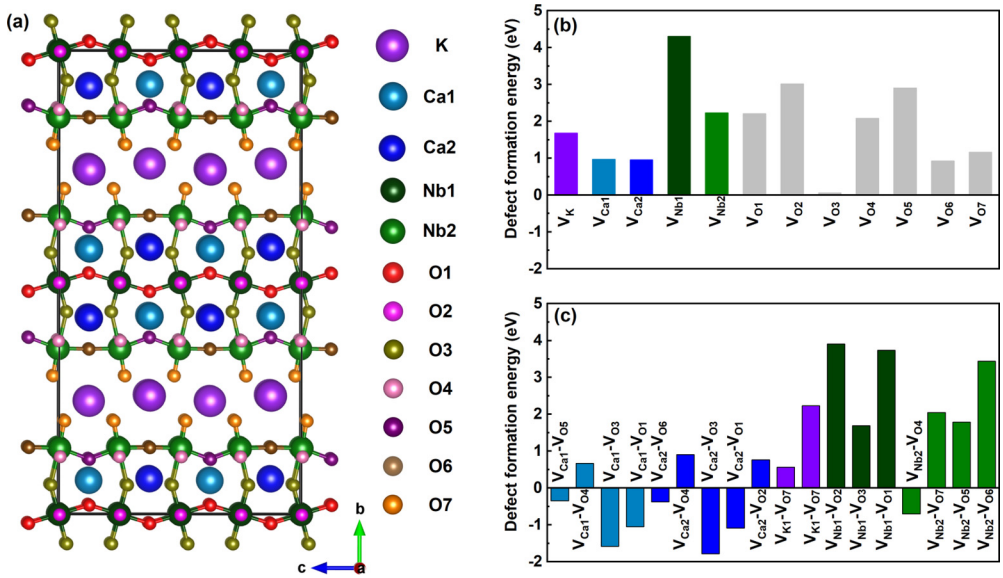

FIG. 3. (a) Schematic structure of the $KCa_2Nb_3O_{10}$ supercell projected along the [1 0 0] direction. The structure is in the orthorhombic *Cmcm* space group, and all atoms are colored according to Wyckoff position. (b) Calculated formation energies of isolated vacancies in $KCa_2Nb_3O_{10}$ and (c) nearest-neighbor cation vacancy-oxygen vacancy pairs.

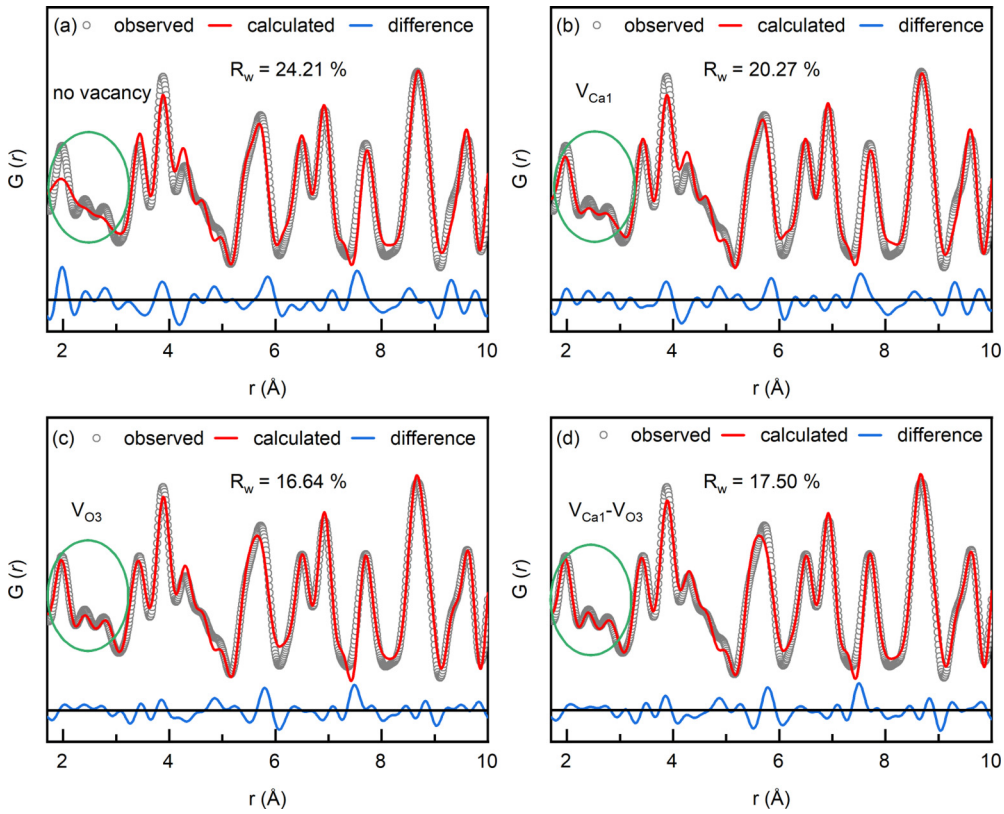

FIG. 4. Observed and calculated $G(r)$ profiles of $KCa_2Nb_3O_{10}$ for interatomic distance $r \leqslant 10$ Å. Note that the calculated structure model is from the density functional theory (DFT) supercell. (a) Supercell with no vacancy; (b) supercell with V_{Ca1}; (c) supercell with V_{O3}; (d) supercell with V_{Ca1}-V_{O3} divacancy pairs.

nearest-neighbor cation-oxygen vacancy pairs, constituting a total of 18 configurations [see the label of Fig. 3(c)].

The formation energy (E_F) of defects is calculated from the total energy of defect supercell ($E_{\text{Defect Supercell}}$) and the total energy of stoichiometric host (E_{Host}) as [43,66]

$$E_F = E_{\text{Defect Supercell}} - E_{\text{Host}} + \sum_i p_i n_i \mu_i, \qquad (2)$$

where μ_i is the chemical potential of species i, their number n_i, and the factor $p_i = -1$ $(+1)$ for atoms added to (removed from) the host to construct the defect supercell. The μ for K, Ca, Nb, and O are derived from the total energies of standard oxides K_2O, CaO, Nb_2O_5, and O_2 molecules, respectively. The formation energies of all the different ionic defects are provided in Table S2 in the Supplemental Material Sec. F 1 [45].

The average E_F of isolated vacancies V_K, V_{Ca}, V_{Nb}, and V_O are 1.68, 0.96, 3.27, and 1.77 eV, respectively (see Table S2 in the Supplemental Material [45]). Among these, the most notable is the V_{O3} vacancy, which is energetically most favorable with $E_F = 0.06$ eV. Therefore, although XPS data did not reveal O deficiency, which is likely due to lower sensitivity and surface adsorbed O, it is expected that O vacancies form in this material. The DFT results also imply that the oxygen vacancy is more likely to appear between the perovskite sublayers, that is V_{O3}, than the interfacial region between the perovskite slab and K atoms. Moreover, analysis of the formation energies of cation-vacancy–oxygen-vacancy pairs shows that V_{Ca}-V_{O3} (Ca includes Ca1 and Ca2) are more probable vacancy complexes than V_{Ca}-V_O (O includes O1, O2, O4, and O5), V_K-V_O, or V_{Nb}-V_O. Importantly, the negative formation energies for V_{Ca}-V_{O3} indicate the likely existence of V_{Ca}-V_{O3} in $KCa_2Nb_3O_{10}$.

In well-known perovskite ferroelectrics, it is traditionally understood that electrical polarization originates from the off-centered displacement of cations from their high-symmetry positions in the crystal lattice [67]. Therefore, a natural question arises on whether local atomic reconstruction around the V_{Ca}-V_O complex gives rise to local dipole moments. To get better insight into this area, we reanalyzed the x-ray $G(r)$ with input from DFT.

D. PDF analysis with input from DFT

The calculated short-range atomic correlations for the structures with cation-oxygen defect complexes are next compared against the experimental $G(r)$. To calculate $G(r)$ from the DFT model structures, the lattice parameters and ADPs were refined to best reproduce the experimental $G(r)$ since the structure calculated from DFT is for 0 K (see details in Supplemental Material Section F.2 [45]). For fitting of $G(r)$ with the inclusion of defect complexes, the displacement correlation parameter δ_2 was not refined since their inclusion only provided marginal improvement in the fit (see Supplemental Material Sec. F 3 [45]). Figures 4(a)–4(d) compare the experimental $G(r)$ with the calculated $G(r)$ based on DFT structures with (a) no vacancy, (b) Ca1 vacancy (V_{Ca1}), (c) O3 (V_{O3}) vacancy, and (d) the V_{Ca1}-V_{O3} divacancy pair.

In Fig. 4(a), the calculated $G(r)$ with no vacancies reproduce the experimentally measured $G(r)$ except for the first three peaks, which correspond to the nearest-neighbor Nb-O and Ca-O/O-O interatomic correlations. The supercells with V_{Ca1} [Fig. 4(b)] or V_{O3} [Fig. 4(c)] isolated vacancies can better reproduce the experimentally measured $G(r)$ than the supercell with no vacancy, which is reflected from lower values of the weighted residuals R_w for these structures and additionally better reproduction of the first three peaks. However, considering electronic charge compensation in cation-vacancy–anion-vacancy pairs and the fact that the samples are highly insulating, the divacancy complex is more likely to form rather than isolated vacancies. Additionally, as can be seen from Fig. 3(c), the divacancy pair of $V_{Ca1(2)}$-V_{O3} has the lowest formation energy (see Table S2 in the Supplemental Material [45]). Moreover, it can be observed from Fig. 4(d) and Figs. S7–S8 in the Supplemental Material [45] that R_w for the supercell structures with V_{Ca1}-V_{O3} are lower than those of structures with V_{Ca1} or V_{Ca2}. Also, R_w for the supercell structures with $V_{Ca1(2)}$-V_{O3} are among the lowest for all the structures, including other isolated vacancy modes, as shown in Fig. S7 in the Supplemental Material [45], and divacancy modes, as shown in Fig. S8 in the Supplemental Material [45]. Therefore, considering both the defect formation energies and reproducibility of the $G(r)$ based on the DFT-calculated supercell structure, we can conclude that the $V_{Ca1(2)}$-V_{O3} divacancies are the predominant defect complex present in the material. In the Kroger-Vink notation, the divacancy pair is represented as $V''_{Ca} - V^{\bullet\bullet}_{O}$; however, here, we use the $V_{Ca1(2)}$-V_{O3} notation without implying their possible ionization states. Similar results about tightly bound cation-oxygen divacancy pairs were obtained earlier for perovskite ferroelectrics in Ref. [68]. However, it is essential to note that the $V_{Ca1(2)}$-V_{O3} divacancy pairs in $KCa_2Nb_3O_{10}$ are oriented nearly orthogonal to the longer b axis. This can be compared with $PbTiO_3$-based perovskite ferroelectrics, where V_{Pb}-V_O are oriented along the longer c axis [37]. Note that, for the fits shown in Fig. 4, the displacement correlation factor δ_2 was not considered. As shown in Fig. S9 in the Supplemental Material Sec. F 3 [45], incorporation of δ_2 while refining the defect structures from DFT yielded only marginal improvements in the fits to the experimental $G(r)$. This suggests that the local structure of $KCa_2Nb_3O_{10}$ is more strongly affected by the ionic defect complexes, as considered here, than due to locally correlated atomic motions.

E. Calculation of vacancy-induced local dipole moment

Figure 5(a) shows the perovskite layers of the $KCa_2Nb_3O_{10}$ supercell with the V_{Ca1}-V_{O3} divacancy pair oriented nearly parallel to the oxygen octahedral layers. The position of the oxygen octahedra and the Nb-O-Nb angle within the different perovskite layers are labeled using D_i^x and β_i^x, where the subscript i refers to their position along the c axis and x denotes their position along the b axis. The distortion parameters (D) for the different O octahedra are represented in Figs. 5(b)–5(d) by solid symbols for the supercell with no vacancy and by open symbols for the supercell with V_{Ca1}-V_{O3} divacancy. The distortion parameter

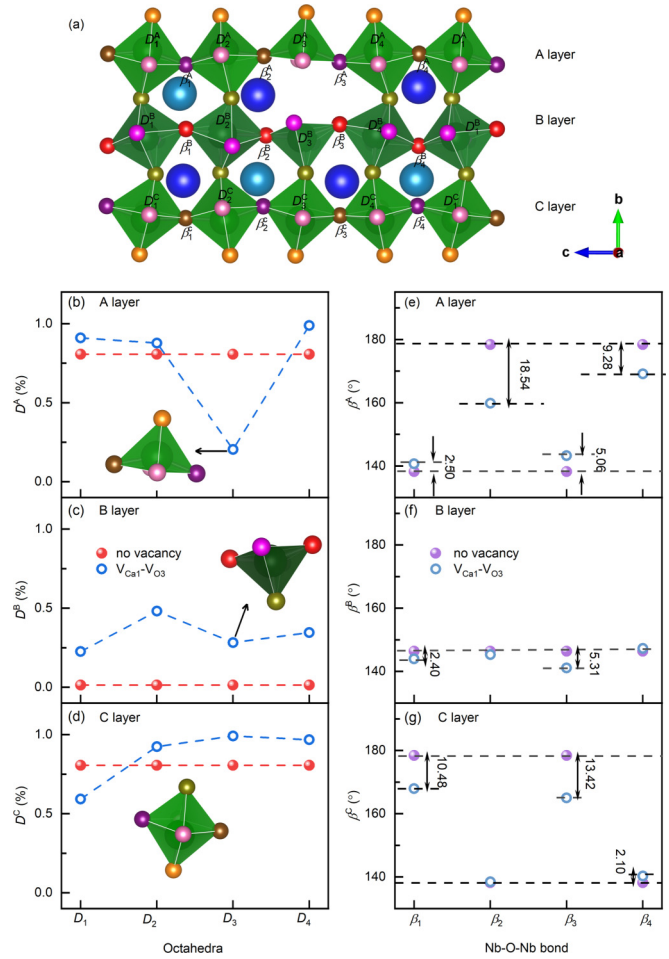

FIG. 5. (a) The triple perovskite slabs of $KCa_2Nb_3O_{10}$ supercell with V_{Ca1}-V_{O3} vacancies. (b)–(d) Distortion parameter evolution in A, B, and C layers, respectively. (e)–(g) Nb-O-Nb angle in a-c plane (angle β) evolution in different perovskite layers A, B, and C, respectively.

(D) is calculated using the following equation [69]:

$$D = \frac{1}{n}\left[\sum_{i}^{n}\left(\frac{d_i - d}{d}\right)^2\right], \tag{3}$$

where n is the coordination number (in this case, $n = 6$), and d_i and d are the individual and average values of the Nb-O bond lengths, respectively. For D_3^A and D_3^B (in Fig. 5), $n = 5$ due to one missing oxygen.

For the structure with no vacancy, the O octahedra in the terminal layers (D_i^A and D_i^C are more distorted ($D \sim 0.81\%$) than the O octahedra in the inner layer (D_i^B) with $D \sim 0.01\%$. With the introduction of the V_{Ca1}-V_{O3} divacancy, all three layers exhibit additional distortion. However, the maximum change in D is observed for D_3^A [see Fig. 5(b) inset], which is closest to the V_{O3} site. Overall, while V_{O3} is placed in between the inner and terminal octahedra, the inner layer exhibits a larger change in D than the terminal layers.

Support for local structural distortions around the defect centers is further obtained from Raman scattering data. Figure 6 shows the Raman spectrum for the synthesized ceramics in the range of wave numbers 400–1000 cm^{-1}. The

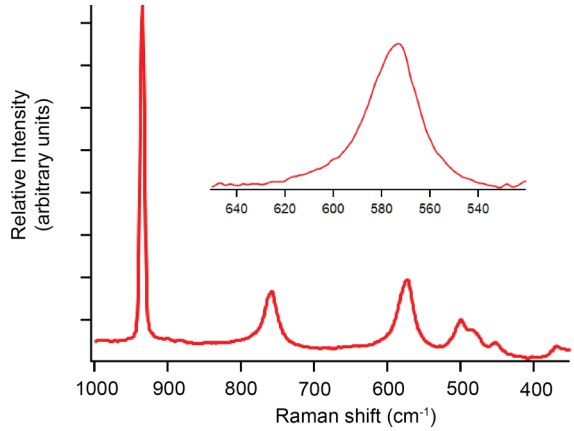

FIG. 6. Raman spectrum of $KCa_2Nb_3O_{10}$ showing significant depletion of terminal short Nb-O bonds (refer to text).

sharp peak at $\sim 935\,\mathrm{cm}^{-1}$ is due to the terminal short Nb-O bond ($\sim$1.7 Å) in the highly distorted octahedra of the terminal layers. In comparison, the peaks at ~ 580 and $\sim 760\,\mathrm{cm}^{-1}$ are due to the Nb-O bonds in the slightly distorted octahedra of the inner layer. The relative number of short Nb-O bonds in the terminal octahedra can be characterized from the intensity ratio $I(\sim 935\,\mathrm{cm}^{-1})/I(\sim 580\,\mathrm{cm}^{-1})$, where I indicates the integrated area under the corresponding peak [70]. Theoretically, for $KCa_2Nb_3O_{10}$, $I(\sim 935\,\mathrm{cm}^{-1})/I(\sim 580\,\mathrm{cm}^{-1})$ should be ~ 2, which reflects the ratio of the terminal octahedra to the inner octahedra [70]. Based on the data shown in Fig. 6, $I(\sim 935\,\mathrm{cm}^{-1})/I(\sim 580\,\mathrm{cm}^{-1}) \sim 1.25$, which indicates a significant depletion of the terminal short Nb-O bonds. The Raman data are consistent with a sharp decrease in D for the terminal octahedron near the V_{Ca}-V_O defect pair, as shown in Fig. 5(b), which is mainly due to the absence of a short Nb-O bond. In addition, the Raman peak at $\sim 580\,\mathrm{cm}^{-1}$ is asymmetric, which indicates inhomogeneous structural distortions for the middle layer octahedra and is likely a result of higher D around defect centers for the structure containing divacancy pairs, as depicted in Fig. 5(c).

The Nb-O-Nb bond angles (β) for the different perovskite layers are shown in Figs. 5(e)–5(g), using the same notation style as D. The solid symbols represent β for the supercell with no vacancy, and the open symbols represent β for the supercell with V_{Ca1}-V_{O3} divacancy pair. With the introduction of V_{Ca1}-V_{O3}, the maximum changes in β are observed for the terminal octahedral layer nearest to the V_{Ca1}-V_{O3} in the A layer, that is, β_2^A. Within the terminal layer of the structure with no vacancy, the tilting angle around the a axis (β) for the neighboring octahedra alternates between 180° and 140°. With the introduction of V_{Ca1}-V_{O3}, the structure relaxes to minimize the difference between β of the neighboring octahedra within the terminal layer. Furthermore, for the inner octahedral layer, β stays close to uniform across the neighboring octahedra, even with the introduction of vacancies. In contrast, D_{1-4}^B are all similarly affected by the introduction of the V_{Ca1}-V_{O3}. This indicates that the additional strain introduced by vacancies is relieved within the inner layer through octahedral distortions rather than by disturbing the octahedral tilting pattern.

Importantly, these results show that introduction of the V_{Ca1}-V_{O3} divacancy modifies the octahedral distortions and tilting by disturbing the complex interplay between the layer-wise strain energies and atomic bonding energies, the details for which will require further investigation. Consequently, although the maximum changes in the octahedral distortions and Nb-O-Nb bond angles occur close to V_{O3}, that is D_3^A and β_2^A, the neighboring positions are also significantly affected. In other words, the modulation of the atomic structure due to the additional strain field from the divacancy pair is longer range (not only limited to nearest neighbors) and therefore not commensurate with the unit cell of the lattice.

The above analysis shows that structural distortions introduced as a result of cation-oxygen divacancies could lead to the formation of local anisotropic electrical dipoles. That is, while the long-range structure is centrosymmetric, the presence of cooperative point vacancies can cause the structure to deviate locally from bulk symmetry and result in uncompensated electrical dipoles. In this regard, we estimated the strength of local polarization of the $KCa_2Nb_3O_{10}$ lattice upon inclusion of V_{Ca}-V_O divacancy pairs from the DFT-relaxed supercell models.

To calculate dipole density, the atomic Born effective charge (BEC) Z_i^* (i = atomic index of the supercell models) was computed using the density functional perturbation theory. BEC is a tensorial quantity; however, the orthorhombic symmetry of the $KCa_2Nb_3O_{10}$ lattice ensures primary contribution from the Z_{xx}^*, Z_{yy}^*, and Z_{zz}^* components. The Cartesian component of the atomic displacement ($d_{x/y/z,i}$) was computed as the difference between the atomic positions in the relaxed defect supercell model and the nondefect supercell model. The magnitudes of polarization density components (P_x, P_y, and P_z) and the effective polarization (P) is then obtained via

$$P_x = \frac{1}{\Omega}\sum_i Z_{xx,i}^* \, d_{x,i}, \quad P_y = \frac{1}{\Omega}\sum_i Z_{yy,i}^* \, d_{y,i},$$

$$P_z = \frac{1}{\Omega}\sum_i Z_{zz,i}^* \, d_{z,i}, \tag{4a}$$

$$|P| = \sqrt{P_x^2 + P_y^2 + P_z^2}. \tag{4b}$$

Here, Ω is the volume of the supercell model. Since the lattice vectors are orthogonal, the Cartesian polarization components P_x, P_y, and P_z match P_a, P_b, and P_c, respectively. The magnitudes of the polarization components are on the order of milli-$e/\mathrm{Å}^2$.

The data for polarization density of V_{Ca}-V_O divacancy pairs are tabulated in Table II. Note that the atoms corresponding to the vacancies are not included in the computation of polarization P, as the BEC of vacancies are essentially zero. Further, the polarization values represent the integrated dipole moments arising from an incommensurate structure due to defect-induced atomic rearrangement. Although we use polarization to describe it, it should not be confused with the conventional polarization definition that is associated with a global structural change or the "ferroelectric phase." Nevertheless, the local polarization plays a vital role in determining the material properties, which is important to characterize. Due to the limited size of our supercell models, the values in Table II can be treated as the theoretical upper bound of

TABLE II. Dipole density obtained from DFT computation using Eq. (4) for relaxed defect supercells with V_{Ca}-V_O nearest-neighbor divacancies.

Sl. No.	Vacancy complex	Dipole density				
		P_a(m e/Å^2)	P_b(m e/Å^2)	P_c(m e/Å^2)	|P|(m e/Å^2)	P(μC/cm^2)
1	V_{Ca1}-V_{O5}	6.270	6.274	6.305	10.883	17.436
2	V_{Ca1}-V_{O4}	0.0	−0.059	−0.033	0.068	0.109
3	V_{Ca1}-V_{O3}	1.614	1.594	1.608	2.780	4.454
4	V_{Ca1}-V_{O1}	2.636	2.675	2.609	4.573	7.327
5	V_{Ca2}-V_{O6}	−0.341	−0.362	−0.314	0.588	0.943
6	V_{Ca2}-V_{O4}	0.0	−0.041	−0.014	0.043	0.069
7	V_{Ca2}-V_{O3}	−5.169	−5.196	−5.186	8.978	14.385
8	V_{Ca2}-V_{O1}	−1.081	−1.107	−1.102	1.899	3.043
9	V_{Ca2}-V_{O2}	−0.001	−0.060	−0.012	0.062	0.099

polarization for $KCa_2Nb_3O_{10}$ that are obtainable with defect dipoles. These values are dependent on the defects under consideration and are significant numerically given that the bulk crystal structure is centrosymmetric. For example, the calculated local polarization of the V_{Ca2}-V_{O3} defect dipole, which has the lowest formation energy and hence is the most probable defect type, is $\sim 14\,\mu C/cm^2$. Compared to the V_{Ca2}-V_O pairs, the polarization of V_{Ca1}-V_{O5} defect has a still larger polarization value $\sim 17\,\mu C/cm^2$, although its formation energy is larger than the other types of defect dipole configuration. These values are expected. For example, consider that the dipole moment of the Pb-O divacancy pair in well-known ferroelectric $PbTiO_3$ is $0.1\,e/Å^2$ or $\sim 160\,\mu C/cm^2$ [37]. In comparison, the polarization values of perovskite ferroelectric compounds $BaTiO_3$ and $PbTiO_3$ are 28.4 and 66 $\mu C/cm^2$, respectively, and that of Aurivillius $Bi_4Ti_3O_{12}$ is 50 $\mu C/cm^2$ [40,71–73].

The synthesized $KCa_2Nb_3O_{10}$ ceramics show large dielectric relaxation at high temperatures as well as dielectric nonlinearity at high electric fields (see Fig. 1), which can be partially attributed to the large local fields from the divacancy pairs. Additional contributions could include space charges at grain boundaries or stacking faults, which are not considered here. The second important observation from the DFT studies is that V_{Ca}-V_O defect dipoles of more than one orientation have similarly negative formation energies, which when integrated within the thermodynamics limits may present no definite directionality but would modulate the magnitude of the macroscopic polarization of bulk $KCa_2Nb_3O_{10}$ ceramics. Recently, Osada *et al.* [5] proposed that deficiency at the A site in nanosheets derived from D-J phases may lead to ferroelectric instability through octahedral distortion and octahedral tilting [10]. Our structural and theoretical analysis provides ample evidence in support of this hypothesis and brings out the role of V_{Ca}-V_O divacancies more distinctly.

IV. CONCLUSIONS

In summary, we obtained the structure of cation-oxygen divacancy pairs in D-J phase layered perovskite $KCa_2Nb_3O_{10}$ by combining x-ray PDF and first-principles computation. Our results indicate that calcium-oxygen divacancy pairs are most likely to form in between the octahedral layers, which gives rise to local structural distortions leading to large dipole moment density that are oriented within the two-dimensional perovskite blocks. Most importantly, the current results demonstrate a strong polar nature of defect-induced local structural distortions in D-J phase compounds, which should motivate a broader investigation of defect dipoles in layered perovskites and their implication on polar interphases or other related macroscopic properties.

ACKNOWLEDGMENTS

Funding support from CityU (Projects No. 7005276 and No. 6000688) are gratefully acknowledged. The work described in this paper was partially supported by a grant from the Research Grants Council of the Hong Kong Special Administrative Region, China (Project No. CityU 11306720). This paper used resources of the Advanced Photon Source, a U.S. Department of Energy (DOE) Office of Science User Facility operated for the DOE Office of Science by Argonne National Laboratory under Contract No. DE-AC02-06CH11357. DFT computations were carried out using the resources provided by the High Performance Computing facility of CityU Burgundy.

[1] C. A.-P. de Araujo, J. D. Cuchiaro, L. D. McMillan, M. C. Scott, and J. F. Scott, Fatigue-free ferroelectric capacitors with platinum electrodes, Nature (London) **374**, 627 (1995).

[2] D. G. Schlom, L.-Q. Chen, X. Pan, A. Schmehl, and M. A. Zurbuchen, A thin film approach to engineering functionality into oxides, J. Am. Ceram. Soc. **91**, 2429 (2008).

[3] C.-H. Lee, N. D. Orloff, T. Birol, Y. Zhu, V. Goian, E. Rocas, R. Haislmaier, E. Vlahos, J. A. Mundy, L. F. Kourkoutis, Y. Nie, M. D. Biegalski, J. Zhang, M. Bernhagen, N. A. Benedek, Y. Kim, J. D. Brock, R. Uecker, X. X. Xi, V. Gopalan *et al.*, Exploiting dimensionality and defect mitigation to create tunable microwave dielectrics, Nature (London) **502**, 532 (2013).

[4] N. A. Benedek, J. M. Rondinelli, H. Djani, P. Ghosez, and P. Lightfoot, Understanding ferroelectricity in layered perovskites: New ideas and insights from theory and experiments, Dalton Trans. **44**, 10543 (2015).

[5] M. Osada and T. Sasaki, Nanoarchitectonics in dielectric/ferroelectric layered perovskites: From bulk 3D systems to 2D nanosheets, Dalt. Trans. **47**, 2841 (2018).

[6] M. Dion, M. Ganne, and M. Tournoux, Nouvelles familles de phases $M^{I}M^{II}{}_{2}Nb_{3}O_{10}$ a feuillets "perovskites", Mater. Res. Bull. **16**, 1429 (1981).

[7] A. J. Jacobson, J. W. Johnson, and J. T. Lewandowski, Interlayer chemistry between thick transition-metal oxide layers: Synthesis and intercalation reactions of $K[Ca_2Na_{n-3}Nb_nO_{3n+1}]$ $(3 \leqslant n \leqslant 7)$, Inorg. Chem. **24**, 3727 (1985).

[8] A. J. Jacobson, J. T. Lewandowski, and J. W. Johnson, Ion exchange of the layered perovskite $KCa_2Nb_3O_{10}$ by protons, J. Less Common Metals **116**, 137 (1986).

[9] B.-W. Li, M. Osada, Y. Ebina, T. C. Ozawa, R. Ma, and T. Sasaki, Impact of perovskite layer stacking on dielectric responses in $KCa_2Na_{n-3}Nb_nO_{3n+1}$ $(n = 3–6)$ Dion-Jacobson homologous series, Appl. Phys. Lett. **96**, 182903 (2010).

[10] B.-W. Li, M. Osada, Y.-H. Kim, Y. Ebina, K. Akatsuka, and T. Sasaki, Atomic layer engineering of high-κ ferroelectricity in 2D perovskites, J. Am. Chem. Soc. **139**, 10868 (2017).

[11] K. Maeda and T. E. Mallouk, Comparison of two- and three-layer restacked Dion-Jacobson phase niobate nanosheets as catalysts for photochemical hydrogen evolution, J. Mater. Chem. **19**, 4813 (2009).

[12] N. Kulischow, C. Ladasiu, and R. Marschall, Layered Dion-Jacobson type niobium oxides for photocatalytic hydrogen production prepared via molten salt synthesis, Catal. Today **287**, 65 (2017).

[13] M. R. Aziza, C.-W. Chang, A. Mohapatra, C.-W. Chu, C.-C. Kaun, and Y.-H. Su, Dion-Jacobson phase perovskite $Ca_2Na_{n-3}Nb_nO_{3n+1}$ $(n = 4–6)$ nanosheets as high-κ photovoltaic electrode materials in a solar water-splitting cell, ACS Appl. Nano Mater. **3**, 6367 (2020).

[14] M. Kato, Y. Imai, T. Kajita, Y. Takarabe, T. Minakawa, K. Nemoto, H. Tezuka, T. Noji, and Y. Koike, Synthesis of oxide superconductors by soft-chemical techniques, Mater. Sci. Eng. B **148**, 53 (2008).

[15] C. J. Fennie and K. M. Rabe, Ferroelectricity in the Dion-Jacobson $CsBiNb_2O_7$ from first principles, Appl. Phys. Lett. **88**, 262902 (2006).

[16] C. Chen, H. Ning, S. Lepadatu, M. Cain, H. Yan, and M. J. Reece, Ferroelectricity in Dion-Jacobson $ABiNb_2O_7$ $(A = Rb, Cs)$ compounds, J. Mater. Chem. C **3**, 19 (2015).

[17] T. Tokumitsu, K. Toda, T. Aoyagi, D. Sakuraba, K. Uematsu, and M. Sato, Powder neutron diffraction study of layered perovskite $KCa_2Nb_3O_{10}$, J. Cer. Soc. Jap. **114**, 795 (2006).

[18] N. A. Benedek, Origin of ferroelectricity in a family of polar oxides: The Dion-Jacobson phases, Inorg. Chem. **53**, 3769 (2014).

[19] T. Zhu, T. Cohen, A. S. Gibbs, W. Zhang, P. S. Halasyamani, M. A. Hayward, and N. A. Benedek, Theory and neutrons combine to reveal a family of layered perovskites without inversion symmetry, Chem. Mater. **29**, 9489 (2017).

[20] E. E. McCabe, E. Bousquet, C. P. J. Stockdale, C. A. Deacon, T. T. Tran, P. S. Halasyamani, M. C. Stennett, and N. C. Hyatt, Proper ferroelectricity in the Dion-Jacobson material $CsBi_2Ti_2NbO_{10}$: Experiment and theory, Chem. Mater. **27**, 8298 (2015).

[21] T. Zhu, A. S. Gibbs, N. A. Benedek, and M. A. Hayward, Complex structural phase transitions of the hybrid improper polar Dion-Jacobson oxides $RbNdM_2O_7$ and $CsNdM_2O_7$ $(M = Nb, Ta)$, Chem. Mater. **32**, 4340 (2020).

[22] A. Pramanick, A. D. Prewitt, J. S. Forrester, and J. L. Jones, Domains, domain walls and defects in perovskite ferroelectric oxides: A review of present understanding and recent contributions, Crit. Rev. Solid State Mater. Sci. **37**, 243 (2012).

[23] Y. Feng, J. Wu, Q. Chi, W. Li, Y. Yu, and W. Fei, Defects and aliovalent doping engineering in electroceramics, Chem. Rev. **120**, 1710 (2020).

[24] V. Thangadurai and W. Weppner, Electrical properties of $A'Ca_2Nb_3O_{10}$ $(A' = K, Rb, Cs)$ layered perovskite ceramics, Ionics **7**, 22 (2001).

[25] R. J. Goff, D. Keeble, P. A. Thomas, C. Ritter, F. D. Morrison, and P. Lightfoot, Leakage and proton conductivity in the predicted ferroelectric $CsBiNb_2O_7$, Chem. Mater. **21**, 1296 (2009).

[26] T. Wang, C.-L. Chiang, P.-C. Li, Y.-K. Hsieh, and C.-F. Wang, Effect of B-site vacancy on surface chemistry and catalytic performance of Dion-Jacobson phase layered perovskite $KCa_2Nb_3O_{10}$, Chem. Eng. J. **244**, 243 (2014).

[27] W. Zhang, K. Fujii, E. Niwa, M. Hagihala, T. Kamiyama, and M. Yashima, Oxide-ion conduction in the Dion-Jacobson phase $CsBi_2Ti_2NbO_{10-\delta}$, Nat. Commun. **11**, 1224 (2020).

[28] E. Siegel and K. A. Müller, Structure of transition-metal—oxygen-vacancy pair centers, Phys. Rev. B **19**, 109 (1979).

[29] E. Siegel and K. A. Müller, Local position of Fe^{3+} in ferroelectric $BaTiO_3$, Phys. Rev. B **20**, 3587 (1979).

[30] W. L. Warren, D. Dimos, G. E. Pike, K. Vanheusden, and R. Ramesh, Alignment of defect dipoles in polycrystalline ferroelectrics, Appl. Phys. Lett. **67**, 1689 (1995).

[31] W. L. Warren, G. E. Pike, K. Vanheusden, D. Dimos, B. A. Tuttle, and J. Robertson, Defect-dipole alignment and tetragonal strain in ferroelectrics, J. Appl. Phys. **79**, 9250 (1996).

[32] D. J. Keeble, B. Nielsen, A. Krishnan, K. G. Lynn, S. Madhukar, R. Ramesh, and C. F. Young, Vacancy defects in (Pb, La)(Zr, Ti)O_3 capacitors observed by positron annihilation, Appl. Phys. Lett. **73**, 318 (1998).

[33] S. Gottschalk, H. Hahn, A. G. Balogh, W. Puff, H. Kungl, and M. J. Hoffmann, A positron lifetime study of lanthanum and niobium doped $Pb(Zr_{0.6}Ti_{0.4})O_3$, J. Appl. Phys. **96**, 7464 (2004).

[34] D. J. Keeble, S. Singh, R. A. Mackie, M. Morozov, S. McGuire, and D. Damjanovic, Cation vacancies in ferroelectric $PbTiO_3$ and Pb(Zr, Ti)O_3: A positron annihilation lifetime spectroscopy study, Phys. Rev. B **76**, 144109 (2007).

[35] Y. Ma, P. Garcia, J. Lechelle, A. Miard, L. Desgranges, G. Baldinozzi, D. Simeone, and H. E. Fischer, Characterization of oxygen defect clusters in UO_{2+x} using neutron scattering and PDF analysis, Inorg. Chem. **57**, 7064 (2018).

[36] A. E. Maughan, A. M. Ganose, A. M. Candia, J. T. Granger, D. O. Scanlon, and J. R. Neilson, Anharmonicity and octahedral tilting in hybrid vacancy-ordered double perovskites, Chem. Mater. **30**, 472 (2018).

[37] C. H. Park and D. J. Chadi, Microscopic study of oxygen-vacancy defects in ferroelectric perovskites, Phys. Rev. B **57**, R13961 (1998).

[38] S. Pöykkö and D. J. Chadi, *Ab initio* study of dipolar defects and 180° domain walls in $PbTiO_3$, J. Phys. Chem. Solids **61**, 291 (2000).

[39] E. Cockayne and B. P. Burton, Dipole moment of a Pb-O vacancy pair in $PbTiO_3$, Phys. Rev. B **69**, 144116 (2004).

[40] K. Co, F.-C. Sun, S. P. Alpay, and S. K. Nayak, Polarization rotation in $Bi_4Ti_3O_{12}$ by isovalent doping at the fluorite sublattice, Phys. Rev. B **99**, 014101 (2019).

[41] B. Jiang and S. M. Selbach, Local and average structure of Mn- and La-substituted $BiFeO_3$, J. Solid State Chem. **250**, 75 (2017).

[42] N. Kitamura, N. Hamao, S. C. Vogel, and Y. Idemoto, Oxide-ion conduction, average and local structures of $LaSrGa_{1-x}Mg_xO_{4-\delta}$ with layered perovskite structure, Electrochemistry **81**, 448 (2013).

[43] S. K. Nayak, H. T. Langhammer, W. A. Adeagbo, W. Hergert, T. Muller, and R. Buttcher, Chromium point defects in hexagonal $BaTiO_3$: A comparative study of first-principles calculations and experiments, Phys. Rev. B **91**, 155105 (2015).

[44] W. A. Adeagbo, H. Ben Hamed, S. K. Nayak, R. Böttcher, H. T. Langhammer, and W. Hergert, Theoretical investigation of iron incorporation in hexagonal barium titanate, Phys. Rev. B **100**, 184108 (2019).

[45] See Supplemental Material at http://link.aps.org/supplemental/10.1103/PhysRevB.104.224104 for additional details on sample preparation, sample composition, measurement and analysis of x-ray scattering data, electrical properties measurements, and DFT calculations.

[46] P. Juhas, T. Davis, C. L. Farrow, and S. J. L. Billinge, PDFGETX3: A rapid and highly automatable program for processing powder diffraction data into total scattering pair distribution functions, J. Appl. Cryst. **46**, 560 (2013).

[47] C. L. Farrow, P. Juhas, J. W. Liu, D. Bryndin, E. S. Bozin, J. Bloch, T. Proffen, and S. J. L. Billinge, PDFFIT2 and PDFGUI: Computer programs for studying nanostructure in crystals, J. Phys. Condens. Matter **19**, 335219 (2007).

[48] J. Rodríguez-Carvajal, Recent advances in magnetic structure determination by neutron powder diffraction, Phys. B: Condens. Matter **192**, 55 (1993).

[49] S.-H. Kweon, M. Im, G. Han, J.-S. Kim, S. Nahm, J.-W. Choi, and S.-J. Hwang, Sintering behavior and dielectric properties of $KCa_2Nb_3O_{10}$ ceramics, J. Eur. Ceram. Soc. **33**, 907 (2013).

[50] R. E. Eitel, T. R. Shrout, and C. A. Randall, Nonlinear contributions to the dielectric permittivity and converse piezoelectric coefficient in piezoelectric ceramics, J. Appl. Phys. **99**, 124110 (2006).

[51] A. Pramanick, D. Damjanovic, J. C. Nino, and J. L. Jones, Subcoercive cyclic electrical loading of lead ziroconate titanate ceramics I: Nonlinearities and losses in the converse piezoelectric effect, J. Am. Ceram. Soc. **92**, 2291 (2009).

[52] A. A. Bokov and Z.-G. Ye, Recent progress in relaxor ferroelectrics with perovskite structure, J. Mater. Sci. **41**, 31 (2006).

[53] J. E. García, R. Pérez, D. A. Ochoa, A. Albareda, M. H. Lente, and J. A. Eiras, Evaluation of domain wall motion in lead zirconate titanate ceramics by nonlinear response measurements, J. Appl. Phys. **103**, 54108 (2008).

[54] H. Fukuoka, T. Isami, and S. Yamanaka, Crystal structure of a layered perovskite niobate $KCa_2Nb_3O_{10}$, J. Solid State Chem. **151**, 40 (2000).

[55] M. S. Seen, D. A. Keen, T. C. A. Lucas, J. A. Hriljac, and A. L. Goodwin, Emergence of Long-Range Order in $BaTiO_3$ from Local Symmetry-Breaking Distortion, Phys. Rev. Lett. **116**, 207602 (2016).

[56] I.-K. Jeong, T. Proffen, F. Mohiuddin-Jacobs, and S. J. L. Billinge, Measuring correlated atomic motion using x-ray diffraction, J. Phys. Chem. A **103**, 921 (1999).

[57] I.-K. Jeong, R. H. Heffner, M. J. Graf, and S. J. L. Billinge, Lattice dynamics and correlated atomic motion from the atomic pair distribution function, Phys. Rev. B **67**, 104301 (2003).

[58] C. L. Farrow, P. Juhas, J. W. Liu, D. Bryndin, E. S. Bozin, J. Bloch, Th. Proffen, and S. J. L. Billinge, *PDFGUI User Guide* (Board of Trustees of Columbia University, New York, 2016).

[59] R. O. Jones and O. Gunnarsson, The density functional formalism, its applications and prospects, Rev. Mod. Phys. **61**, 689 (1989).

[60] M. C. Payne, M. P. Teter, D. C. Allan, T. A. Arias, and J. D. Joannopoulos, Iterative minimization techniques for *ab initio* total-energy calculations: Molecular dynamics and conjugate gradients, Rev. Mod. Phys. **64**, 1045 (1992).

[61] J. P. Perdew, K. Burke, and M. Ernzerhof, Generalized Gradient Approximation Made Simple, Phys. Rev. Lett. **77**, 3865 (1996).

[62] P. E. Blöchl, Projector augmented-wave method, Phys. Rev. B **50**, 17953 (1994).

[63] H. J. Monkhorst and J. D. Pack, Special points for Brillouin-zone integrations, Phys. Rev. B **13**, 5188 (1976).

[64] G. Kresse and J. Furthmüller, Efficiency of *ab initio* total energy calculations for metals and semiconductors using a plane-wave basis set, Comput. Mater. Sci. **6**, 15 (1996).

[65] G. Kresse and J. Furthmüller, Efficient iterative schemes for *ab initio* total-energy calculations using a plane-wave basis set, Phys. Rev. B **54**, 11169 (1996).

[66] S. K. Nayak, C. J. Hung, V. Sharma, S. P. Alpay, A. M. Dongare, W. J. Brindley, and R. J. Hebert, Insight into point defects and impurities in titanium from first principles, npj Comput. Mater. **4**, 11 (2018).

[67] M. E. Lines and A. M. Glass, *Principles and Applications of Ferroelectrics and Related Materials* (Oxford University Press, Oxford, 1977).

[68] H. Mestric, R.-A. Eichel, T. Kloss, K.-P. Dinse, S. Laubach, S. Laubach, P. C. Schmidt, K. A. Schönau, M. Knapp, and H. Ehrenberg, Iron-oxygen vacancy defect centers in $PbTiO_3$: Newman superposition model analysis and density functional calculations, Phys. Rev. B **71**, 134109 (2005).

[69] L. Veselinović, M. Mitrić, M. Avdeev, S. Marković, and D. Uskoković, New insights into $BaTi_{1-x}Sn_xO_3$ $(0 \leqslant x \leqslant 0.20)$ phase diagram from neutron diffraction data, J. Appl. Cryst. **49**, 1726 (2016).

[70] J. M. Jehng and I. E. Wachs, Structural chemistry and Raman spectra of niobium oxides, Chem. Mater. **3**, 100 (1991).

[71] H. H. Wieder, Electrical behavior of barium titanatge single crystals at low temperatures, Phys. Rev. **99**, 1161 (1955).

[72] V. G. Bhide, M. S. Hegde, and K. G. Deshmukh, Ferroelectric properties of lead titanate, J. Am. Ceram. Soc. **51**, 565 (1968).

[73] D. Maurya, A. Charkhesht, S. K. Nayak, F.-C. Sun, D. George, A. Pramanick, M.-G. Kang, H.-C. Song, M. M. Alexander, D. Lou, G. A. Khodaparast, S. P. Alpay, N. Q. Vinh, and S. Priya, Soft phonon mode dynamics in Aurivillius-type structures, Phys. Rev. B **96**, 134114 (2017).